


Quasiparticle self-consistent GW band structures and phase transitions of LiAlO_2 in tetrahedrally and octahedrally coordinated structures

Phillip Popp  and Walter R. L. Lambrecht 

Department of Physics, Case Western Reserve University, 10900 Euclid Avenue, Cleveland, Ohio 44106-7079, USA

 (Received 17 May 2022; revised 25 July 2022; accepted 8 September 2022; published 11 October 2022)

A first-principles computational study is presented of various phases of LiAlO_2 . The relative total energies and equations of state of the α , β , and γ phases are determined after structural relaxation of each phase. The β and γ tetrahedral phases are found to be very close in energy and lattice volume with the γ phase having the lowest energy. The octahedral α phase is a high-pressure phase and the transition pressure from the γ and β phases to α is determined to be about 1 GPa. The electronic band structures of each phase at their own equilibrium volume are determined using the quasiparticle self-consistent (QS) GW method as well as using the 0.8Σ approach in which the QSGW self-energy is reduced by a factor of 0.8 to correct for the underscreening of W in QSGW. The effective masses of the band edges and the nature of the band gaps are presented. The lowest energy γ phase is found to have a pseudodirect gap of 7.69 eV. The gap is direct at Γ but corresponds to a dipole forbidden transition. The imaginary part of the dielectric function and the absorption coefficient are calculated in the long-wavelength limit and the random phase approximation, without local field or electron-hole interaction effects for each phase, and their anisotropies are discussed. Si doping on the Al site is investigated as a possible n -type dopant in γ - LiAlO_2 using a 128-atom supercell corresponding to 3.125% Si on the Al sublattice in the generalized gradient approximation and a smaller 16-atom cell with 25% Si in the QSGW approximation. The Si is found to significantly perturb the conduction band and lower the gap but a clearly separated deep donor defect level is not found. However, the donor binding energy is still expected to be relatively deep, on the order of a few tenths eV in the hydrogenic effective mass approximation.

DOI: [10.1103/PhysRevMaterials.6.104605](https://doi.org/10.1103/PhysRevMaterials.6.104605)

I. INTRODUCTION

LiAlO_2 is a ceramic material that is known to occur in at least five crystal structures: rhombohedral α - LiAlO_2 (space group $R\bar{3}m$, No. 166) [1], orthorhombic β - LiAlO_2 (space group $Pna2_1$, No. 33) [2], tetragonal γ - LiAlO_2 (space group $P4_12_12$, No. 92) [3], and tetragonal δ - LiAlO_2 (space group $I4_1/amd$, No. 141) [4,5]. Among these, both β and γ forms are tetrahedrally coordinated while α and δ are octahedrally coordinated. The δ form is essentially a slightly disordered rocksalt-type phase, in which the $4a$ Wyckoff positions are about 80% occupied with Al, 20% Li, and with the roles of Al and Li reversed on the $4b$ positions. A fully disordered ϵ cubic phase has also been reported [5]. A 48-atom cell with space group $P\bar{4}m2$ is listed in Materials Project [6] and provides an approximate computational model for these disordered rocksalt-type phases.

LiAlO_2 has been investigated for applications in tritium breeding in fusion reactors [7,8], as a matrix in molten carbonate fuel cells [9], and as a substrate for GaN light-emitting diodes (LEDs) due to the small lattice mismatch between γ - LiAlO_2 and GaN [10]. Moreover, LiAlO_2 is closely related to LiGaO_2 —another ceramic material that is also known to adopt $R\bar{3}m$ and $Pna2_1$ structures and that has recently become of interest as a possible ultrawide-band-gap (UWBG)

semiconductor due to suggestions that LiGaO_2 could be n -type doped by silicon or germanium [11–15]. Various experimental works have found the band gap of LiGaO_2 in the range 5.26–5.6 eV [16–19], and quasiparticle self-consistent GW (QSGW) [20] calculations predict a gap of 5.81 eV [21]. We expect LiAlO_2 to have an even larger band gap than LiGaO_2 .

LiAlO_2 has recently also been considered in the context of Li-ion batteries. It was used as a coating to protect LiCoO_2 [22] but Li was also found to diffuse in LiAlO_2 itself at high temperatures [23,24], and solid solutions of LiAlO_2 with LiMO_2 , where M is a transition metal, were proposed by Ceder *et al.* [25]. LiAlO_2 has also been used as an additive in composite electrolytes [26]. For a more complete literature overview of these recent applications, see Singh *et al.* [27]. The phase transitions of LiAlO_2 at high temperature are important in this context and were studied by Singh *et al.* [27] as well as the pressure-induced transitions we consider here.

The electronic structure and phase transitions of LiAlO_2 have already been studied to some extent. The structure of γ - LiAlO_2 at ambient pressure and temperature was determined experimentally by Marezio via Cu $K\alpha$ and Mo $K\alpha$ radiation photographs [3]. The $\gamma \rightarrow \delta$ phase transition has been studied experimentally [4,5], and Sailuam *et al.* [28] have carried out a first-principles computational study of the band structures and pressure-induced $\gamma \rightarrow \delta$ phase transition [28]. Ma *et al.* have done a first-principles study of α - LiAlO_2 [1]. Singh *et al.* [27] did an extensive computational study

*walter.lambrecht@case.edu

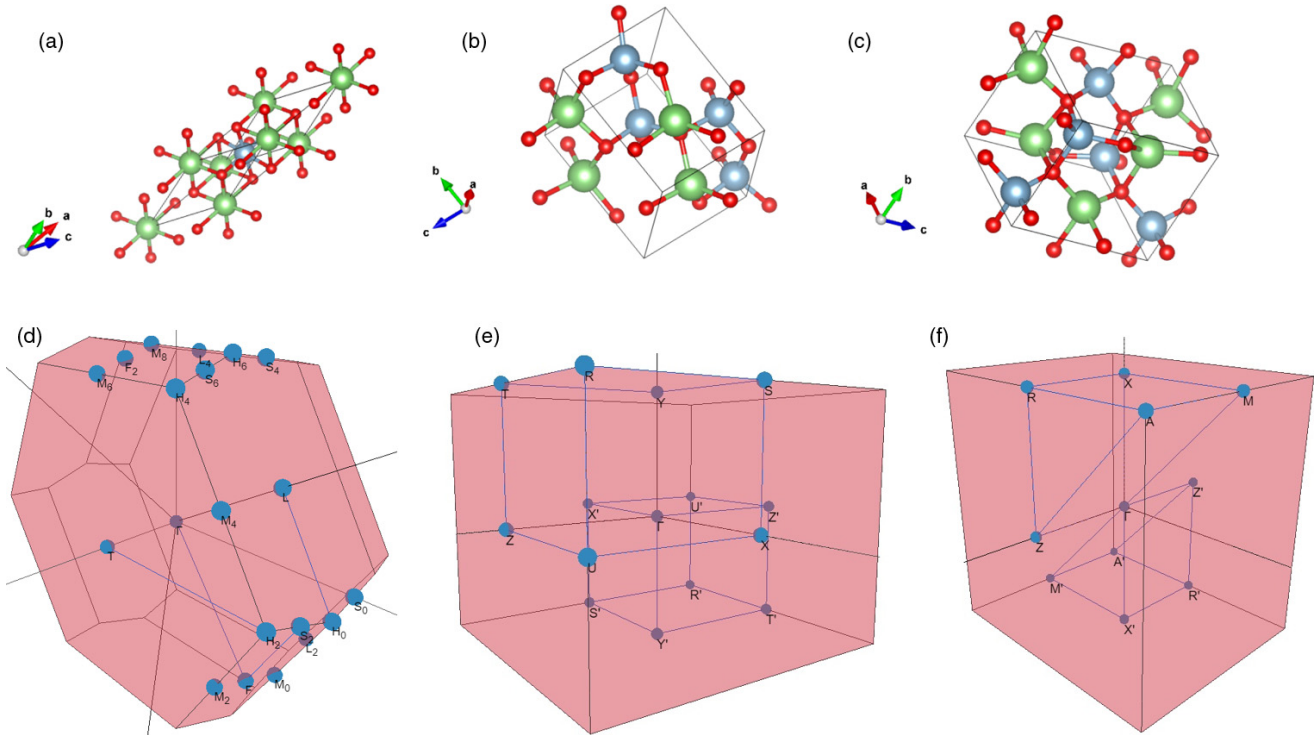


FIG. 1. [(a)–(c)] Crystal structures (made with VESTA [34]) and [(d)–(f)] Brillouin zones (made with SEEK-PATH [35]) of α -, β -, and γ -LiAlO₂. Spheres indicate Li (green), Al (blue), and O (red).

of the temperature-pressure phase diagram and also reported electronic band structures of the various phases. However, there still remain open questions, especially on the electronic structure. With the exception of the study by Sailuam *et al.* [28], prior first-principles works have largely used density functional theory (DFT) methods with local or semilocal exchange-correlation functionals, which are well known to significantly underestimate band gaps. Sailuam *et al.* [28] obtained a gap of 6.56 eV for γ -LiAlO₂ using the Heyd-Scuseria-Ernzerhof (HSE) hybrid functional, much larger than previous DFT studies. We seek to further improve upon these estimates using the more accurate QSGW method. Not only the band gap but other details of the band structure, such as the direct or indirect nature of the gap and the effective masses, are relevant to the potential semiconductor applications, which have not yet received attention. Thus, our paper is focused on the electronic structure and its properties relevant to potential but not yet explored applications of the material as an active semiconductor. Therefore, we will also briefly consider the possibility of doping.

In relation to the band gap and optoelectronic properties, we point out that Huang *et al.* [29] determined an optical absorption onset from transmission of VIS-UV to occur at 191 nm, indicating a gap of ~ 6.5 eV consistent with Zou *et al.* [30], who also measured a drop in transmission near 190 nm. More recently, Holston *et al.* [31,32] measured optical defects in LiAlO₂ induced by radiation of doping with Cu. They also did not see any absorption in as-grown crystals above 200 nm wavelength. From these we can deduce that the optical gap appears to be near 6.5 eV at room temperature. Besides optical properties, they also report electron paramagnetic resonance (EPR) spectra of these defects.

The lowest-energy and most thermally stable form of LiAlO₂ is the γ phase, but coexistence of the α and γ phases is a common result of syntheses performed below 973 K [33], and surface contamination of bulk γ -LiAlO₂ with β -LiAlO₂ is known to occur as a result of matching between the a and b axes of the orthorhombic β phase with the a and c axes of the tetragonal γ phase [2]. Therefore, we consider each of the α , β , and γ phases. Additionally, the $R\bar{3}m$ structure was found to be a high-pressure phase of LiGaO₂ [21], so it is also interesting to study α -LiAlO₂ for the sake of comparing these two closely related materials. We omit here the δ phase because it is actually a disordered phase, which requires larger cells to model, and the octahedral coordination is already represented by the α phase. While other work in the literature [27] has already studied phase transitions extensively, it is useful to compare our results to their work. The structures studied in this paper and their Brillouin zones are shown in Fig. 1.

II. COMPUTATIONAL METHODS

The structure relaxation calculations in this work are performed using the QUANTUM ESPRESSO pseudopotential plane-wave implementation of DFT [36]. We use projector augmented-wave pseudopotentials for all QUANTUM ESPRESSO calculations [37]. The exchange-correlation energy was treated in the generalized gradient approximation (GGA) using the Perdew-Burke-Ernzerhof (PBE) parametrization [38]. For each of the α , β , and γ phases, we start with the lattice parameters provided by Materials Project [6] where available. The unit cell is relaxed at a range of volumes around the equilibrium volume, and the cohesive energy per formula

unit is calculated from the total energy at self-consistency and the reference energies of the free atoms (not including spin-polarization corrections of the atom). Bulk moduli and first derivatives of the bulk moduli with respect to pressure are then extracted for each phase by fitting the corresponding energy vs volume points to the energy curve obtained from integrating the Birch-Murnaghan equation of state [39] via nonlinear least squares. Transition pressures between different phases are then extracted from these fits via the common tangent method. The structural relaxation results for the internal coordinates were further checked with the all-electron full-potential linearized muffin-tin orbital (FP-LMTO) method as implemented in the QUESTAAL code [40] while keeping the lattice constant ratios fixed. The obtained energy ordering of the phases was found to be consistent with QUANTUM ESPRESSO results provided the same muffin-tin radii were kept for all phases.

To overcome the limitations of semilocal DFT for band gaps, we use the many-body-perturbation theoretical *GW* method [41]. The band structure calculations performed here use the quasiparticle self-consistent version of the *GW* method [20] (QSGW) as implemented in the QUESTAAL code [40]. The *G* in *GW* represents the one-particle Green's function, and the *W* represents the screened Coulomb interaction. The QSGW approach is independent of the DFT starting point Hamiltonian H^0 , because a nonlocal exchange-correlation potential is extracted from the *GW* self-energy, in the form of its matrix in the basis set of H^0 eigenstates $\tilde{\Sigma}_{nm} = \frac{1}{2}\text{Re}[\Sigma_{nm}(\epsilon_n) + \Sigma_{nm}(\epsilon_m)]$ where Re indicates taking the Hermitian part, and is used to update H^0 and iterated to convergence. At each iteration $\Sigma(\omega) = iG^0(\omega) \otimes W(\omega)$ with \otimes standing for convolution. At convergence, the quasiparticle energies of *GW* become equal to the Kohn-Sham eigenvalues of the updated H^0 . This approach is known to give much more accurate band gaps than semilocal DFT but is known to systematically overestimate the band gaps slightly because the screening of *W* is calculated in the random phase approximation and thereby underestimates screening by not including electron-hole interaction effects. This shortcoming can be overcome by including ladder diagrams [42,43] but this is still a rather expensive approach and it was found that reducing the self-energy correction $\tilde{\Sigma} - v_{xc}^{DFT}$ by a universal factor 0.8, which we call 0.8Σ , provides a practical alternative [44,45].

The main factors that determine the accuracy and convergence of the FP-LMTO implementation of the QSGW method [20] include the basis-set choice and the \mathbf{k} -point mesh on which the self-energy is calculated. In the FP-LMTO method we use augmented spherical waves with smoothed Hankel functions as radial functions outside the spheres and typically use a basis set with two sets of Hankel function energies and smoothing radii. Here we use an *spdfspd* basis set on each of the atoms, which means one set of smoothed Hankel functions includes orbitals up to *f* and the second up to *d* spherical harmonics. The smoothing radii and energies are chosen in a standard way by fitting these radial wave functions to the tail of the free atom eigenstates. The basis functions are expanded to $l_{\max} = 4$ within each augmentation sphere. To further test the convergence, we added high-energy *s* and *p* local orbitals but found them to affect the band gap

TABLE I. Convergence parameters for QSGW band structure calculations; E_{Σ}^{\max} is the maximum energy up to which the self-energy $\Sigma(\omega)$ is calculated.

Phase	\mathbf{k} mesh	E_{Σ}^{\max} (Ry)
α	$6 \times 6 \times 6$	3.9
β	$3 \times 3 \times 3$	3.5
γ	$3 \times 3 \times 3$	3.4

negligibly. The two-point quantities, such as the bare and screened Coulomb interaction *W*, are represented in a separate basis set of Bloch functions which include products of partial waves inside the spheres and plane waves projected on the interstitial region. This basis set is far more efficient than a plane-wave basis set at representing the screening within the Hilbert space of the bands of interest and thereby also reduces the need to include high-lying empty states in calculating the polarization propagator *P* used in $W = v + vPW$ with *v* the bare Coulomb interaction and in the calculation of Σ . The mixed product basis set and interstitial plane-wave basis functions in the QSGW scheme are expanded to G_{\max} of 2.7 Ry^{1/2} and 3.3 Ry^{1/2}, which are standard values.

The final (i.e., after checking convergence) \mathbf{k} -meshes and energy cutoffs for Σ used in the QSGW calculations for each phase are given in Table I. In the QSGW iterations the $\tilde{\Sigma}$ is replaced by an average value between E_{Σ}^{\max} and $E_{\Sigma}^{\max} - 0.5$ Ry. The atom-centered LMTO basis set provides a natural interpolation scheme for the self-energy matrix to a finer \mathbf{k} -point mesh used in the charge-potential self-consistency iterations and for obtaining the bands along the symmetry lines. It thus provides accurate band dispersions and also effective masses. For details about the QSGW implementation we refer the reader to the method description papers [20,40].

III. RESULTS

A. Equations of state and transition pressures

We begin with an investigation of the structural properties and high-pressure phase transitions of α -, β -, and γ -LiAlO₂. For the α and γ phases, we use as initial input the lattice constants and site positions provided by Materials Project [6]. However, at the time of our investigation, Materials Project did not have structural information for β -LiAlO₂, so we instead use the data for LiGaO₂ in the *Pna2*₁ structure and then relax the unit cell substituting aluminum for gallium.

First, we discuss the fitted energy vs volume curves shown in Fig. 2 and transition pressures between structures. We fit our directly calculated energies as functions of volume to the energy obtained from integrating the Birch-Murnaghan equation of state, which is given by [39]

$$E(V) = E_0 + \frac{9V_0B_0}{16} \left\{ \left[\left(\frac{V_0}{V} \right)^{2/3} - 1 \right]^3 B'_0 + \left[\left(\frac{V_0}{V} \right)^{2/3} - 1 \right]^2 \left[6 - 4 \left(\frac{V_0}{V} \right)^{2/3} \right] \right\}, \quad (1)$$

where E is the total energy in the crystalline state, E_0 is the total energy of the neutral free atoms at rest, V is the volume of the unit cell, V_0 is the equilibrium volume of the unit cell,

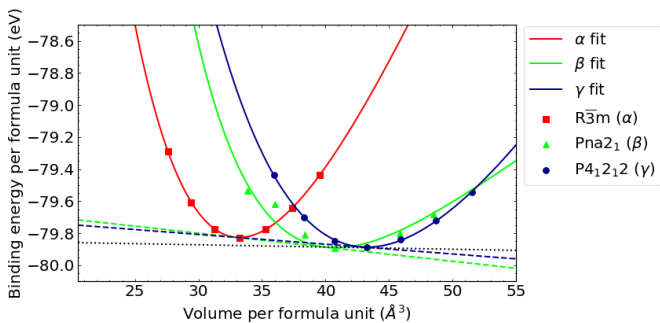


FIG. 2. Directly calculated energy vs volume points and equation of state fits for α -, β -, and γ -LiAlO₂, along with common tangents corresponding to the $\beta \rightarrow \alpha$ (green dashed) and $\gamma \rightarrow \alpha$ (blue dashed) and $\gamma \rightarrow \beta$ (black dotted) high-pressure phase transitions.

B_0 is the bulk modulus, and B'_0 is the first derivative of the bulk modulus with respect to pressure.

We calculate the transition pressures between different structures using the common tangent construction, wherein the negative of the slope of the tangent line is the pressure required to achieve enthalpic equality between two crystal structures. A plot of the directly calculated points and equation of state fits is shown in Fig. 2, and values of the fitting parameters B_0 and B'_0 along with the transition pressures are given in Table II. From Fig. 2, it is evident that the α phase is a high-pressure form of the material. This result is analogous to that obtained by Radha *et al.* from their analysis of LiGaO₂, which found the $R\bar{3}m$ structure to be a high-pressure phase of that material [21]. Further, the γ phase is the lowest-energy structure, though the difference between the energy minima in the β and γ phases is only $\sim 10^{-4}$ eV, which is consistent with experimental observation of these two phases coexisting. Their lattice volume per formula unit are also close but slightly larger for γ , indicating that also β could be stabilized under pressure. The common tangents shown in Fig. 2 indicate a tetrahedral to octahedral transition around 0.98 GPa for $\gamma \rightarrow \alpha$ and 1.4 GPa for $\beta \rightarrow \alpha$.

These results agree well with those of Singh *et al.* [27], who also found the β and γ phases to have very close energy minima and establish a $\gamma \rightarrow \alpha$ transition at ~ 1.3 GPa. They obtain this by calculating the energy and enthalpy directly as a function of pressure, by explicitly imposing the pressure as a stress tensor as independent variable in their calculation, whereas we start from the energy-volume curves and use the

TABLE II. Fitting parameters corresponding to Fig. 2: B_0 , bulk modulus at equilibrium; B'_0 , pressure derivative of the bulk modulus at equilibrium volume; p_t is the transition pressure.

Phase	B_0 (GPa)	B'_0	p_t (GPa)
α	136	3.64	
β	70.5	6.01	1.4 ^a
γ	90.2	3.14	0.98, ^b 0.22 ^c

^a $\beta \rightarrow \alpha$.

^b $\gamma \rightarrow \alpha$.

^c $\gamma \rightarrow \beta$.

common tangent construction, but in principle, these procedures should give equivalent results. They also mention that in the range 0–1.2 GPa the β structure already has lower enthalpy. We calculate a transition pressure of 0.22 GPa for $\gamma \rightarrow \beta$ based on the fitted equations of state.

The study by Singh *et al.* [27] is more complete than ours in terms of the phase diagrams by their inclusion of temperature and entropy effects and by also considering the higher pressure transitions to the δ phase but for low temperatures our results agree well with theirs. Previously, Sailuam *et al.* [28] studied the $\gamma \rightarrow \delta$ transition and found a transition pressure of about 2–3 GPa depending on which functional was used. This agrees qualitatively with Singh *et al.* [27]. They did not consider the α phase but did evaluate energy barriers between the phases as a function of pressure. We preferred here to focus on the basic tetrahedral-to-octahedral phase transition by considering the simpler α phase. After all, the δ phase, which is a disordered cubic phase with tetragonal distortion, is not as well established structurally or can only approximately be described by a small unit cell because of the fractional occupations of lattice sites.

For reference, we give the equilibrium lattice constants of each phase in Table III as obtained from the QUANTUM ESPRESSO minimization. These are used later for the electronic structure on which we focus. For the α phase, we here use the primitive rhombohedral cell parameters a and the opening angle between the three equal size lattice vectors. To compare with the hexagonal conventional cell, used in the work by Singh *et al.* [27], which is three times larger in volume, note that $a_h = \sqrt{2}a_r\sqrt{1 - \cos\alpha}$ and $c_h = 3a_r\sqrt{1 + 2\cos\alpha}/\sqrt{3}$. This gives $a_h = 2.82$ Å and $c_h = 14.36$ Å, in good agreement with the values by Singh *et al.* [27].

It is also interesting to study how the lattice parameters themselves change as functions of unit cell volume. For the rhombohedral α structure the volume of the unit cell is given by $V = a^3\sqrt{1 - 3\cos^2\alpha + 2\cos^3\alpha}$. Figure 3(a) shows that the opening angle α between each pair of lattice vectors decreases with increasing volume. For the β structure we can see in Fig. 3(b) that b/a and c/a stay more or less constant as the volume is decreased until the volume approaches the region where the phase transition to the α phase occurs. The sudden change in these ratios indicates the incipient instability of the β structure and is possibly related to the transition path between wurtzite and rocksalt suggested in Ref. [46]. Likewise in the γ structure, the c/a ratio is seen to increase when approaching the transition volume but otherwise stays constant and b/a stays equal to 1 as required by symmetry. We have checked that, during the relaxation procedure, the symmetries required by each lattice were maintained.

B. Band structures

For our final band structure calculations, we use the lattice parameters corresponding to the lowest-energy point on each of the equation-of-state fits of Fig. 3, i.e., those given in Table III.

The QSGW 0.8 Σ approximation band structure of α -LiAlO₂ is shown over a wide energy range in Fig. 4, with corresponding plots of the partial densities of states (resolved by ℓ) in both the valence and conduction bands shown in

TABLE III. Space groups, lattice constants, volume per formula unit, and Wyckoff positions for different phases of LiAlO₂.

Structure Space group	α $R\bar{3}m$	β $Pna2_1$	γ $P4_12_12$
	$a = 5.06 \text{ \AA}$ $\alpha = 32.47^\circ$ $V = 33.2 \text{ \AA}^3$	$a = 5.29 \text{ \AA}$ $b = 6.28 \text{ \AA}$ $c = 4.90 \text{ \AA}$ $V = 40.7 \text{ \AA}^3$	$a = 5.24 \text{ \AA}$ $c = 6.31 \text{ \AA}$ $V = 43.3 \text{ \AA}^3$
Li	$1a$ (0,0,0)	$4a$ ($x = 0.0837, y = -0.3761, z = -0.0033$)	$4a$ ($x = -0.1858, y = -0.1858, z = 0$)
Al	$1b$ ($\frac{1}{2}, \frac{1}{2}, \frac{1}{2}$)	$4a$ ($x = 0.0786, y = 0.1262, z = 0.0048$)	$4a$ ($x = 0.1768, y = 0.1768, z = 0$)
O	$2c$ ($\pm u, \pm u, \pm u$) $u = 0.2381$	$4a$ ($x = 0.0614, y = 0.1053, z = 0.3654$)	$8b$ ($x = 0.3392, y = 0.2904, z = -0.2271$)
O _{II}		$4a$ ($x = 0.1003, y = -0.3528, z = 0.4062$)	

Fig. 5. We find that the α phase has an indirect gap of 9.30 eV, with the conduction band minimum occurring at the Γ point. The indirect nature is already present also in the GGA band structure. From the partial densities of states, we can discern that the deep-lying bands spanning ~ -20 to ~ -17.5 eV are those derived primarily from the oxygen $2s$ orbitals. The higher-lying valence states from ~ -5 to 0 eV are primarily due to the oxygen $2p$ -derived bands, though there are contributions from both aluminum $3s$ and $3p$ as well because these are bonding states with the cation atomic orbitals. The lowest-lying (around 10 eV) conduction states consist of a mixture of lithium $2s$, (antibonding) oxygen $2s$ and $2p$, and aluminum $3s$ orbitals. At higher energy, there are peaks corresponding to significant lithium $2s$, oxygen $2p$, and aluminum $3p$ contributions. This confirms the ionic picture in which Li donates its electrons to the oxygen.

We now turn to a magnified view of the valence states near the Fermi level, shown in Fig. 6. This shows that two almost equal energy valence band maxima (VBM) occur between Γ and L and Γ and S_0 . The nomenclature for the high-symmetry points follows the convention of the Bilbao crystallographic server website [47] and is also given in Fig. 1. The conduction band minimum (CBM) meanwhile is at Γ and the material thus has an indirect band gap. At Γ the VBM is doubly degener-

ate and has E_u symmetry of the D_{3d} point group, which is (x, y) -like while the state below it is nondegenerate with A_{1u} symmetry, which is z -like. This indicates that direct vertical transitions from the VBM at Γ to the conduction band which has A_{1g} symmetry (s -like) are dipole allowed for polarization perpendicular to the threefold-symmetry axis, while the transitions from the crystal field split-off state will occur for polarization along the symmetry axis. This is confirmed by the optical absorption calculations discussed below. However, the indirect gap is about 0.1 eV lower than the direct gap. One may notice some avoided band crossings just below the VBM along Γ - T , Γ - L , and Γ - S_0 . These were checked by using a fine spacing of the \mathbf{k} -points along the lines and indicate that these bands belong to the same irreducible representation of the group of \mathbf{k} along these lines and can therefore not cross.

The band structure of the β structure is shown in Figs. 7–9. The ℓ -resolved partial densities of states are shown in Fig. 10. The overall orbital character of the bands is the same as in the α structure. The zoom-in near the VBM shows again an indirect band gap, which is also already present in the GGA. The VBM occurs near the point T , which is (0,0.5,0.5) in units of the reciprocal lattice vectors. An even closer magnification shown in Fig. 9 right near the T point in the directions T - Z and T - R shows that T is a saddle point with a minimum in

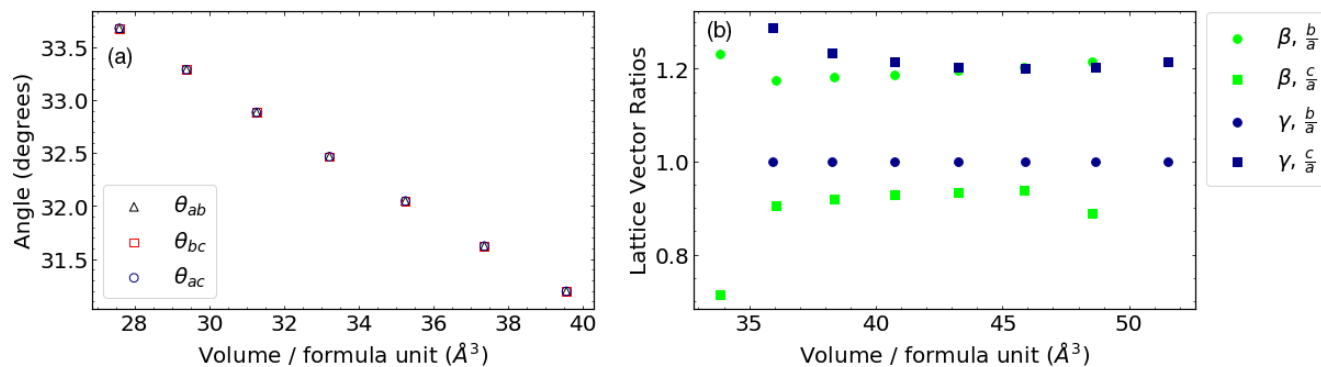


FIG. 3. (a) Lattice angles vs volume for α -LiAlO₂ (we use θ_{ab} , θ_{bc} , and θ_{ac} to denote the lattice angles instead of the traditional α , β , and γ to avoid confusion with the phase labeling of LiAlO₂). (b) $\frac{b}{a}$ and $\frac{c}{a}$ ratios vs volume for tetrahedrally coordinated β - and γ -LiAlO₂.

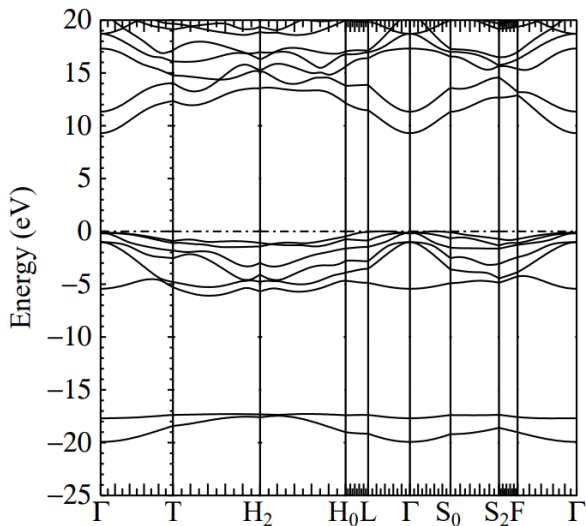


FIG. 4. QSGW 0.8Σ band structure of α -LiAlO₂ spanning a wide range of valence and conduction states.

the T - Z direction and a maximum along T - R . The line along T - Z contains two maxima close in energy to one another. It also is at a maximum in the T - Y direction. Thus, great care is required to determine the effective mass tensor at the actual VBM. The VBM at Γ lies ~ 0.24 eV below it. The valence

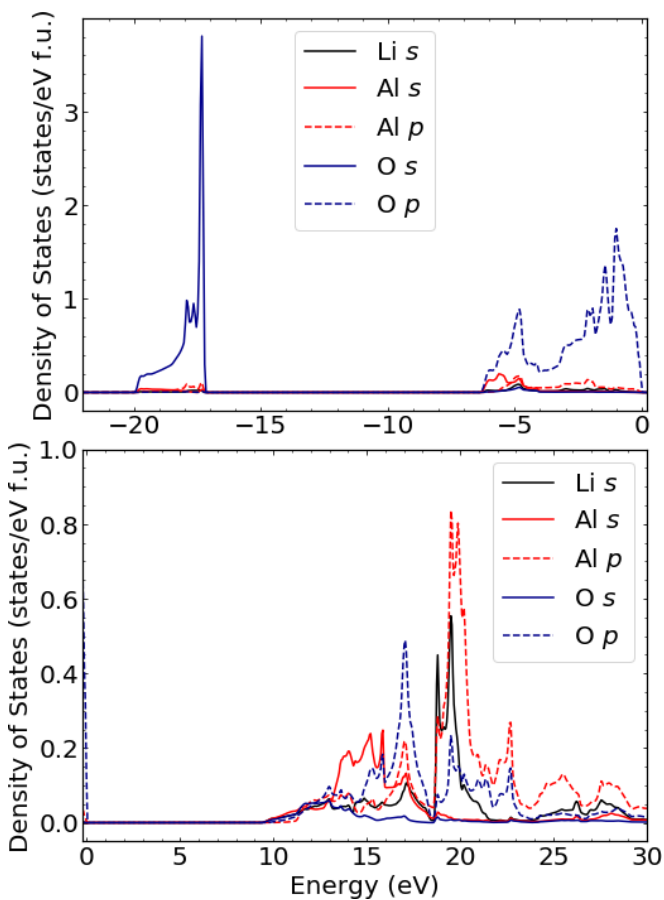


FIG. 5. ℓ -resolved partial densities of states in α -LiAlO₂ in the (top) valence and (bottom) conduction bands.

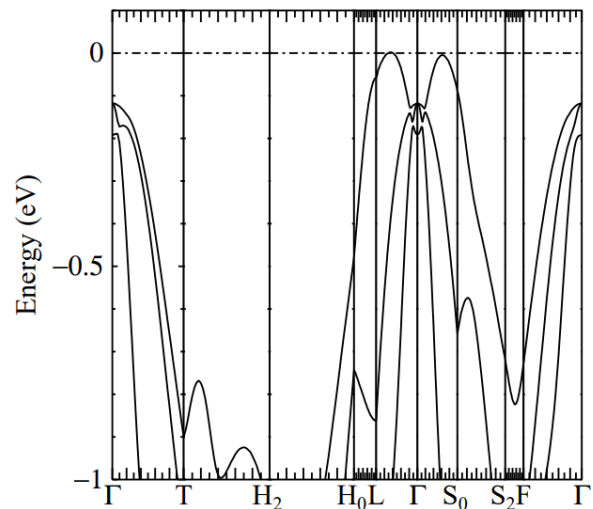


FIG. 6. Magnified view of the high-lying valence states of the QSGW 0.8Σ band structure of α -LiAlO₂.

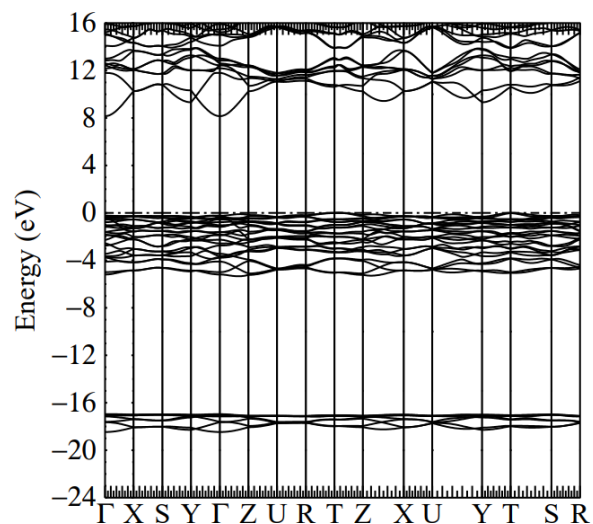


FIG. 7. QSGW 0.8Σ band structure of β -LiAlO₂ spanning a wide range of valence and conduction states.

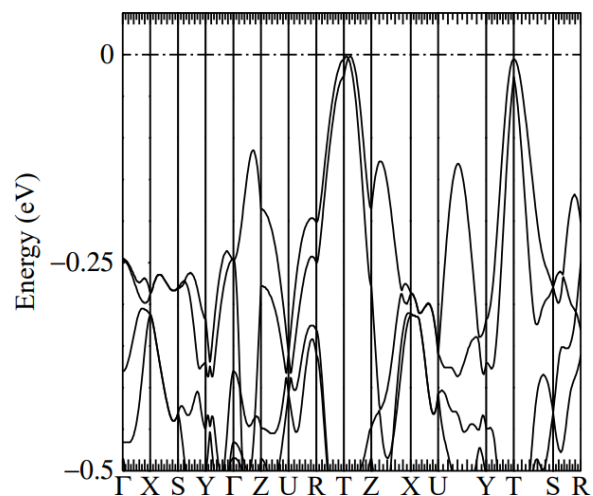


FIG. 8. Magnified view of the high-lying valence states of the QSGW 0.8Σ band structure of β -LiAlO₂.

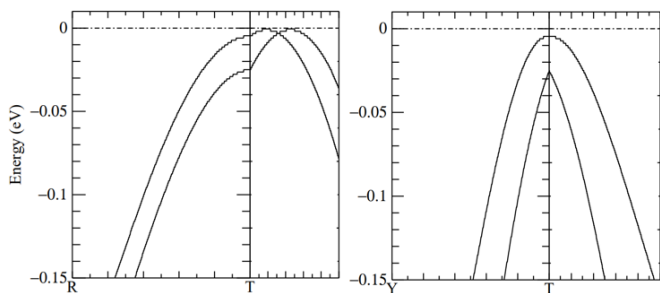


FIG. 9. Close magnifications on the saddle point at T and the actual VBM along T - Z in the valence bands of β - LiAlO_2 . The left panel shows the topmost bands along R - T - Z and the right panel shows the topmost bands along Y - T - S .

bands at Γ from the highest one and down have irreducible symmetries, a_2, a_1, b_1, b_2 , which are respectively forbidden, allowed for z, x, y polarization for transitions to the a_1 symmetry CBM at Γ . These symmetry labels were determined by inspection of the eigenvectors.

Finally, for the γ structure, the band structure is shown in Figs. 11 and 12, with the ℓ -resolved partial densities of states in Fig. 13. The overall orbital character of the bands is similar to the α and β phases. The magnification shows that this phase

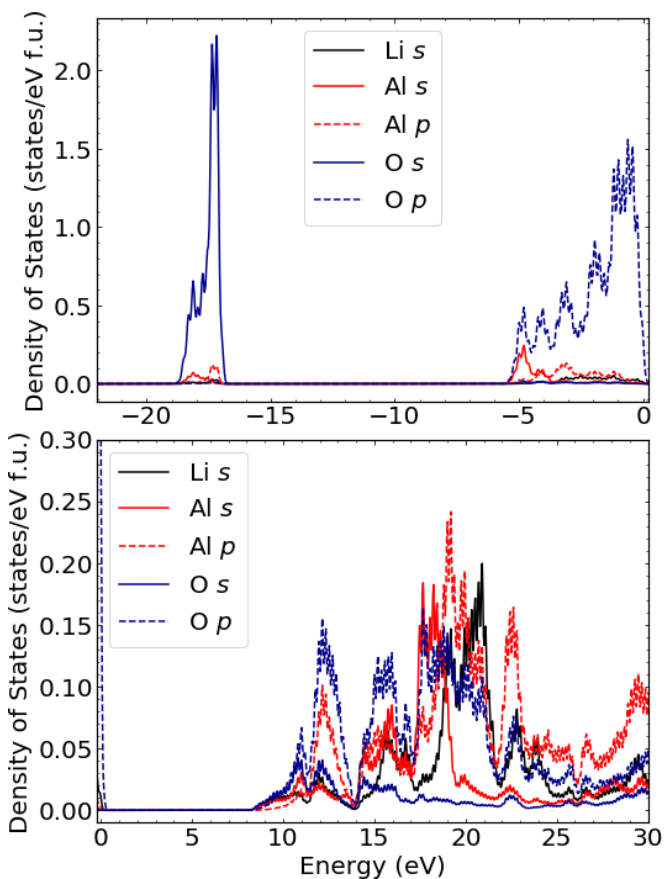


FIG. 10. ℓ -resolved partial densities of states in β - LiAlO_2 in the (top) valence and (bottom) conduction bands. A Gaussian broadening with a width of 0.1 eV was applied to these spectra to better distinguish some of the features.

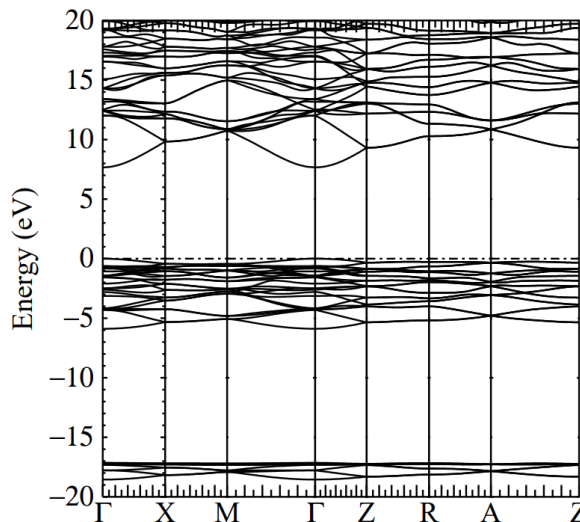


FIG. 11. QSGW 0.8Σ band structure of γ - LiAlO_2 spanning a wide range of valence and conduction states.

has a direct band gap. The CBM has A_1 symmetry but the VBM has B_1 symmetry in the point group D_4 . This implies that the gap is pseudodirect. In other words, it is direct but dipole forbidden. The next lower VBM at Γ is double degenerate and therefore has E symmetry but lies about 0.63 eV lower. However, along Γ - X the group of \mathbf{k} is C_2 and contains the C_{2x} symmetry axis under which B_1 is even. This means direct vertical transitions for states along the Γ - X axis become allowed for z polarization because both CBM and VBM at these points and z are even or belong to the A irreducible representation of C_2 . Meanwhile, along Γ - M , the group of \mathbf{k} is also C_2 but contains the C_2 axis along the (110) direction, under which B_1 is odd. This implies that vertical transitions from the valence band along Γ - M to the conduction band become allowed for x or y polarization because the CBM is still even under that C_2 operation. In other words, the VBM has irreducible representation (irrep) B while the CBM has irrep A and transitions are allowed for x or y because these

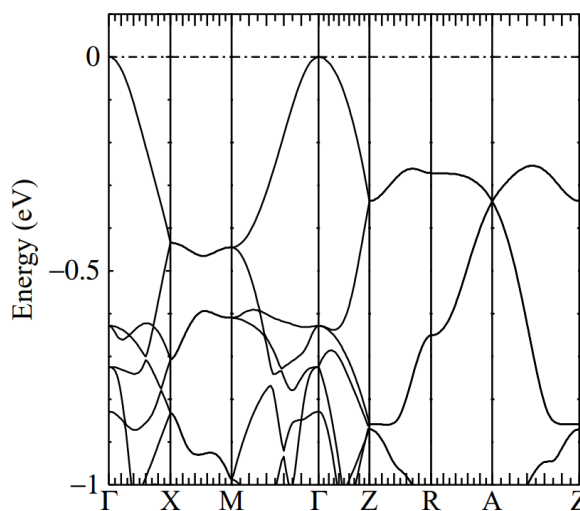


FIG. 12. Magnified view of the high-lying valence states of the QSGW 0.8Σ band structure of γ - LiAlO_2 .

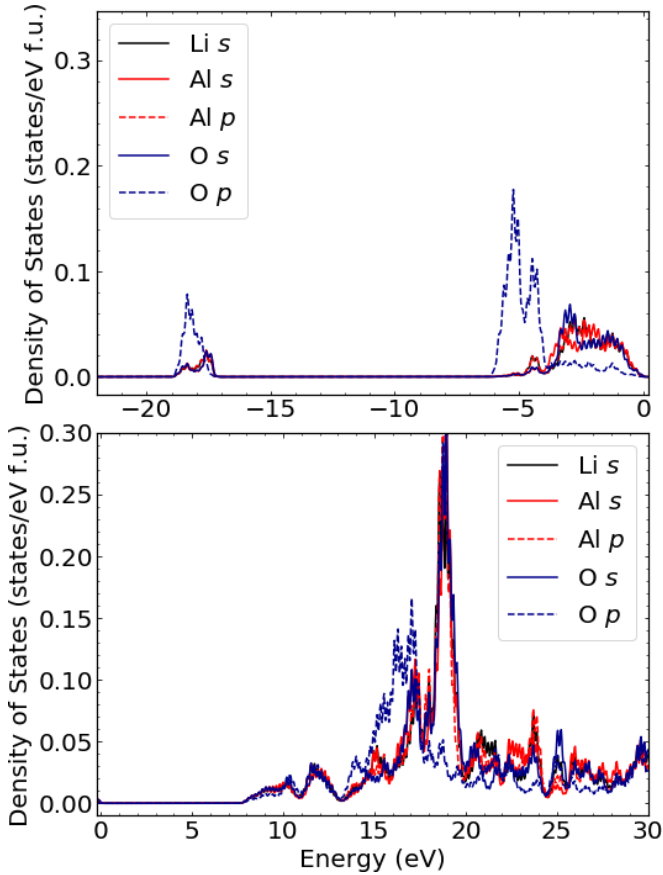


FIG. 13. ℓ -resolved partial densities of states in γ -LiAlO₂ in the (top) valence and (bottom) conduction bands. A Gaussian broadening with a width of 0.1 eV was applied to these spectra to better distinguish some of the features.

belong to the B irrep. Along Γ - Z the group of \mathbf{k} is C_4 and the top valence band belongs to the B irreducible representation and thus the transitions are still forbidden. We will see that thus both x and y polarization should be allowed for energies slightly above the direct gap at Γ but also very close to it for transitions for z polarization.

The band gaps of all three phases are summarized in Table IV. Our GGA band gaps of 4.48 eV for γ and 6.18 eV for α agree reasonably with Singh *et al.*'s [27] 4.7 and 6.2 eV, respectively. Qualitatively, the differences in gap between the different structures agree well with prior work in the sense that the β structure has only slightly higher gap than γ but the octahedral phases have a significantly larger gap. The QSGW gaps of course are significantly larger and are more reliable. In terms of details of the band structure, prior work missed

TABLE IV. Band gaps of α -, β -, and γ -LiAlO₂ from various approximations, of which QSGW 0.8 Σ is expected to be the most accurate.

Phase	GGA	QSGW	QSGW 0.8 Σ
α	6.18 eV	10.1 eV	9.30 eV
β	4.93 eV	8.94 eV	8.16 eV
γ	4.48 eV	8.47 eV	7.69 eV

TABLE V. Effective electron masses at the VBMs and CBMs of α -, β -, and γ -LiAlO₂, extracted from the band curvatures near the extremal points.

Phase/extreme point	m_{xx} (m_e)	m_{yy} (m_e)	m_{zz} (m_e)
α (VBM) ^a	-6.6	-0.69	-2.8
α (CBM)	0.47	0.47	0.58
β (VBM)	-1.3	-0.57	-0.94
β (CBM)	0.43	0.39	0.36
γ (VBM)	-1.7	-1.7	-2.9
γ (CBM)	0.41	0.41	0.44

^aPrincipal values of the mass tensor. The masses labeled x and z actually correspond to principal axes 15° from the crystal axes.

the indirect nature of the gap in the α and β structures. For the α structure, they used the conventional hexagonal cell and hence show the bands in the corresponding hexagonal Brillouin zone. They may thus have missed the points where the actual VBM occurs. Second, for all three phases, they only show a band structure on a large energy scale, where the top valence bands are very flat and therefore it is difficult to ascertain where the actual VBM occurs.

C. Effective masses

The curvature of the bands near the band edges provides the effective masses, which are important for transport properties. They are summarized in Table V.

As expected from the symmetries of the α and γ phases, the Γ point CBM of the α phase and CBM and VBM of the γ phase have effectively one transverse and one longitudinal effective mass. The valence band masses are significantly higher than the conduction band masses as is evident from the flat top valence band. For the β phase they were determined by zooming in very closely to the actual VBM along T - Z , as shown in Fig. 10. Note that we here give electron masses, so the negative signs for the VBM indicate positive hole masses.

D. Optical absorption

The imaginary part of the dielectric function $\epsilon_2(\omega)$, which is proportional to the optical absorption coefficient, was calculated in the long-wavelength independent particle approximation, ignoring local field and excitonic effects, according to

$$\epsilon_2(\omega) = \frac{8\pi^2 e^2}{\Omega \omega^2} \sum_v \sum_c \sum_{\mathbf{k} \in BZ} f_{v\mathbf{k}} (1 - f_{c\mathbf{k}}) \times |\langle \psi_{v\mathbf{k}} | [H, \mathbf{r}] | \psi_{c\mathbf{k}} \rangle|^2 \delta(\omega - \epsilon_{c\mathbf{k}} + \epsilon_{v\mathbf{k}}), \quad (2)$$

where the commutator $[H, \mathbf{r}]$ gives the band velocity and includes the contributions from the nonlocal self-energy, and $\epsilon_{v\mathbf{k}}$ and $\epsilon_{c\mathbf{k}}$ are the valence and conduction band states at \mathbf{k} obtained in the QSGW method. The $f_{i\mathbf{k}}$ are the band occupation numbers (Fermi functions at zero temperature) and are 1 for $n = v$ and 0 for $n = c$. Ω is the volume of the unit cell.

These functions are shown in Figs. 14–16 for the α , β , and γ phases, respectively, along with the real parts of the dielectric function $\epsilon_1(\omega)$ and the absorption coefficients $\alpha(\omega)$.

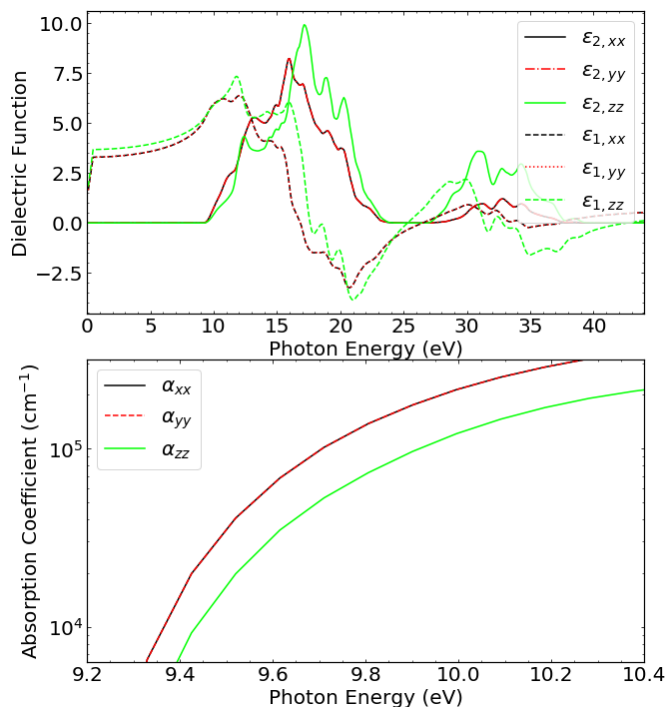


FIG. 14. Top: Real (ϵ_1) and imaginary (ϵ_2) components of the dielectric function for α -LiAlO₂. Bottom: Optical absorption coefficients in logarithmic scale near the onset of absorption.

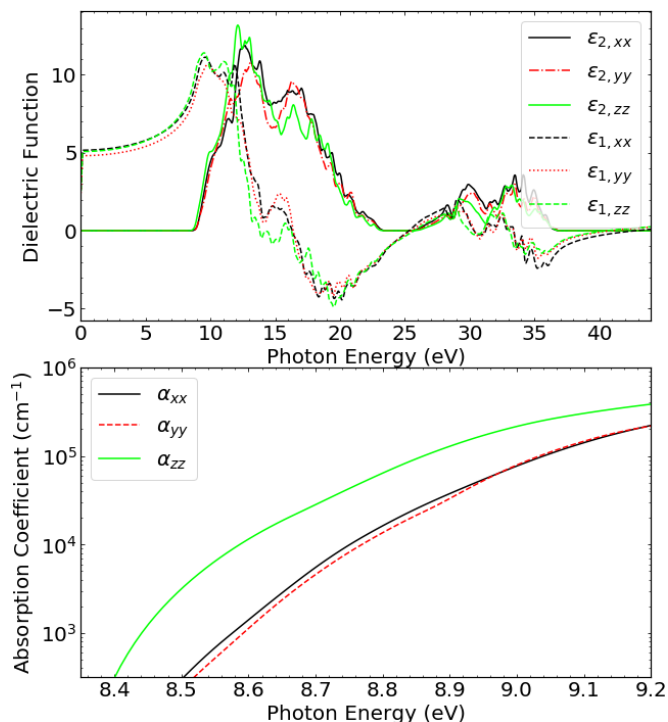


FIG. 15. Top: Real (ϵ_1) and imaginary (ϵ_2) components of the dielectric function for β -LiAlO₂. Bottom: Optical absorption coefficients in logarithmic scale near the onset of absorption.

The real parts are obtained from the imaginary parts via a Kramers-Kronig transformation, and the optical absorption from the relation $\alpha(\omega) = 2\epsilon_2(\omega)/n(\omega)$, where $n(\omega)$ is the real part of the index of refraction $\tilde{n}(\omega) = \sqrt{\epsilon_1(\omega) + i\epsilon_2(\omega)}$. The onsets of absorption and their respective polarizations are consistent with the symmetry analysis in the previous section. For α , the top VBM at Γ is E -like and hence has allowed transitions for x, y polarizations, while the VBM-1 has A_1 symmetry and hence has allowed transitions for z polarization. For β the top VBM at Γ is forbidden but very close to the a_1 symmetry level allowed for z ; the next ones have b_1 corresponding to x and b_2 corresponding to y symmetries and hence the onset occurs in the order z, x, y . For the γ structure the top valence band at the Γ transition to the CBM is forbidden, but transitions along Γ - X become allowed for z polarization and along Γ - M for x, y polarization. This is consistent with the calculated onsets of absorption. Because the matrix elements are expected to gradually increase as \mathbf{k} moves away from Γ either along Γ - X or Γ - M the onset of optical transitions would not follow the usual $\sqrt{E - E_0}$ behavior for direct allowed transitions but rather an $(E - E_0)^{3/2}$ behavior, where E_0 is the onset of transitions. On the other hand, even for the direct allowed transitions in the β case, the expected $\sqrt{E - E_0}$ behavior is only seen very close to the onset. This is because the conduction band at somewhat higher energies above the CBM becomes linear in \mathbf{k} , in which case, the $\epsilon_2(\omega)$ will turn over to become proportional to ω^2 . In the γ phase we have a combination of linearly increasing matrix elements and a conduction band that turns from parabolic to linear behavior, but, in any case, it is clear from the figures that the absorption coefficient turns on slower for the γ than for the β case.

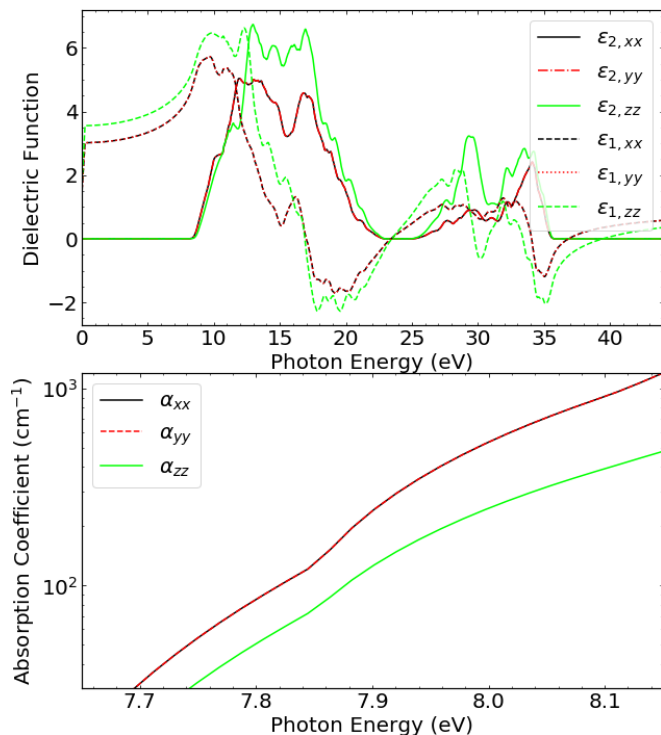


FIG. 16. Top: Real (ϵ_1) and imaginary (ϵ_2) components of the dielectric function for γ -LiAlO₂. Bottom: Optical absorption coefficients in logarithmic scale near the onset of absorption.

At present, no experimental data on the optical absorption or dielectric function over the range we have calculated are available. This is not surprising given the difficulty to obtain adequate light sources in this deep UV range, which is only available at synchrotrons. As mentioned already in the Introduction, there were two prior experimental studies [29,30] which showed a decrease in transmission at about 190 nm or 6.5 eV for the γ phase. No data are available for the high-pressure phases. These onsets of absorption are significantly lower than the quasiparticle band gaps calculated here. There are two possible reasons for this discrepancy: first, finite temperature effects and zero-point motion of the band gap and, second, excitonic effects. In a very ionic material, as we have here, excitonic effects can be expected to be large and could substantially reduce the optical absorption onset from the band-to-band onset. An initial estimate can be made within the hydrogenic Wannier exciton model. Using a reduced mass of 0.33 and a dielectric constant of about 3.5, the binding energy would be 0.36 eV. On the other hand, electron-phonon coupling band gap renormalization effects could also be substantial, leading to a zero point motion correction and even larger reductions at room temperature. A full calculation of these effects is beyond the scope of the present paper. However, comparing to other ionic oxides like MgO suggests the finite temperature effects could well be of order 0.5 eV. Combining this with the estimated exciton binding energy a reduction by about 0.9–1.0 eV would bring the absorption onset down to 6.7 eV, in reasonable agreement with experiment. Finally, we should point out that the optical measurements carried out thus far had a cutoff at about 190 nm in the UV and only a start of the reduction of transmission was measured at this wavelength. The nature of the absorption onset, which we here predict to be forbidden direct, is therefore still unclear but is challenging to measure with standard available light sources in the UV. Furthermore, defect-related absorption band tails can often lead to an underestimate of the band gap.

E. Silicon doping of γ -LiAlO₂

With band gaps larger than 7 eV, the utility of LiAlO₂ in ultrawide-band-gap (UWBG) semiconductor applications will depend heavily on whether it can successfully be doped. Otherwise, it is just another insulator. The electrical conductivity is also of importance in the context of Li diffusion and the opportunities for LiAlO₂ as electrodes in Li batteries. For successful *n*-type doping one must find a dopant which leads to shallow donor levels in the gap and can be readily introduced in the material. For example, Si is used as an *n*-type dopant in GaN but in Al_xGa_{1-x}N alloys of high Al content $x > 0.8$ leads to a deep donor due to a distortion of the defect structure away from the simple substitutional cation site [48], which is called a DX-type defect. Donor binding energies larger than a few tenths of an eV are usually considered ineffective for doping. Inspired by prior work on LiGaO₂ [15], we consider Si doping in LiAlO₂.

In this section we present the results of a band structure calculation for γ -LiAlO₂ doped with silicon as a candidate *n*-type dopant. First, we simply replaced one Al in the 16-atom unit cell by Si, which corresponds to 25% doping. While this is an unrealistically high doping level, the advantage is that we

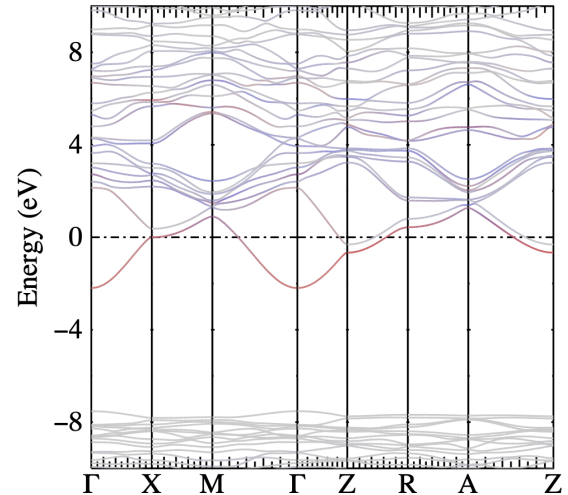


FIG. 17. Band structure of SiAl₃O₈ in the γ structure and in the QSGW approximation. The red (blue) color indicates the Si *s* (Si *p*) orbital contributions with background bands in grey.

can readily perform the calculation at the QSGW level. Next, we studied a 128-atom $2 \times 2 \times 2$ supercell, with a single Si_{Al} corresponding to 3.125% of the Al cation sublattice. We first calculate it at the GGA level. Finally, we use a recently developed cut-and-paste approach [49] to obtain approximately the QSGW band structure in the 128-atom cell with a single Si, from the real-space self-energy of the perfect crystal and the self-energy matrix of the Si atom and its neighbors from the 16-atom QSGW calculation. In this approach we use a cutoff of the real-space self-energy matrices of 6.27 Å. Figure 17 shows the results of the 16-atom cell. The Fermi level now lies about 2 eV above the CBM, indicating that no new levels occur in the gap and the additional electron just starts to fill the conduction band. However, the bottom of the conduction band is clearly strongly Si dominated and the QSGW gap at 5.33 eV is significantly lower than that of pure γ -LiAlO₂. This might at first sight indicate that the Si may actually introduce a deep donor level, which is here broadened into an impurity band because of the high Si concentration and merging with the conduction band. We need a larger cell to refute this possibility.

The results for the 128-atom cell are shown in Fig. 18. We here show only two directions of the Brillouin zone. The faint red color of the lowest three conduction bands indicates their small Si *s* contribution. The background color for the bands without any Si *s* was chosen as a light grey because otherwise it would obscure the red color. The lowest three conduction bands both have some Si *s* contribution but it is less pronounced because the Si concentration is lower and the Fermi level now lies only 0.67 eV above the CBM. These bands essentially are the folded version of the conduction band of the 16-atom cell in the Brillouin zone of the supercell, which has half the size in each direction, although at the new Brillouin zone edge, a gap opens. The band gap between the O 2*p*-like VBM and the Si-like CBM is about 7.28 eV and is close to that of the corresponding perfect crystal gap of 7.43 eV. It is here a little bit lower than the converged value of Table IV because of the real-space cutoff of the self-energy.

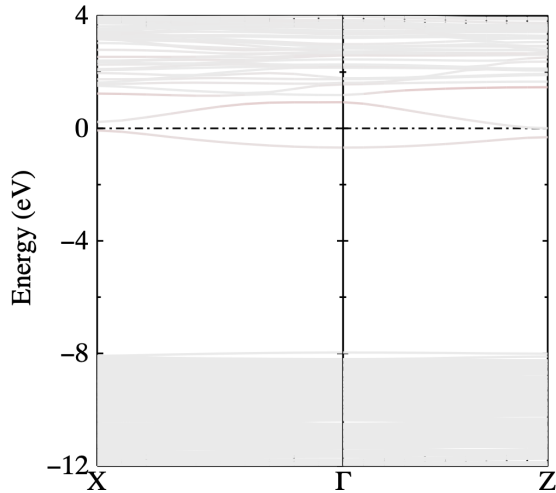


FIG. 18. Band structure of γ -LiAlO₂:Si in a 128-atom supercell in the cut-and-paste QSGW method. The red color indicates Si *s*-like orbital contribution.

Thus the Si still pushes the CBM slightly down but less so than in the 16-atom cell and there is no evidence of a deep donor level. Compared to the corresponding GGA results, the CBM is simply pushed up along with its Si contribution. These results did not include relaxation of the structure. However, relaxation of the nearest-neighbor O atoms around the Si show an inward relaxation of the Si-O bonds by about 6%. They do not indicate a strong distortion or DX center formation. Indeed, it did not lead to any notable difference in the band structure in the GGA, which still does not show a defect level to emerge in the gap.

These results indicate *n*-type doping should be possible. However, the hydrogenic donor model would predict $E_B = m_c^* R / \epsilon^2$, which, with R the Rydberg unit (13.6057 eV), $m_c^* \approx 0.4$ and $\epsilon \approx 3.5$, gives $E_B \approx 0.4$ eV. This estimate includes only electronic screening. Estimating the phonon contributions to the screening requires the calculation of longitudinal optical (LO) phonons, which we have not yet done. However, comparison with LiGaO₂ indicates a static dielectric constant of about 6.5 is expected. This would reduce the donor binding energy to about 0.1 eV. This shows that even if Si doping does not produce a well-separated defect band in the gap in a first-principles calculation in the cell size we can here accommodate, it will likely act as a relatively deep donor with order of 100 meV binding energy. This is similar to LiGaO₂ for which experimental confirmation of *n*-type doping also is still to be accomplished but promising enough to warrant experimental attempts to dope these materials with Si. While these

estimates indicate efficient *n*-type doping may be challenging for both LiGaO₂ and LiAlO₂, they would significantly extend the gap range of UWBG semiconductors. Some compromise between efficiency of doping and larger band gaps may be necessary. For comparison, in β -Ga₂O₃, the conduction band effective mass is about 0.3 and the dielectric constant about 10, giving a binding energy of order 40 meV. The expected donor binding energy in LiGaO₂ and LiAlO₂ are thus relatively high but, on the other hand, still smaller than typical acceptor binding energies related to *p*-type doping in, for example, GaN.

IV. CONCLUSIONS

The main conclusions of this paper are as follows. First, in terms of structures, the γ phase has the lowest energy but is very close to the β phase, which may already be stabilized at slight pressures of about 0.2 GPa. A phase transition from these tetrahedrally bonded phases to the octahedrally bonded α phase is predicted to occur near 1 GPa. The band structures of the three phases were obtained in the QSGW method and yield band gaps larger than 7 eV with a pseudodirect gap of 7.69 eV in the γ phase, indirect gap of 8.16 eV in the β phase, and indirect gap of 9.30 eV in the α phase. The calculated onset of absorption in the γ phase, slightly above the pseudodirect gap of 7.7 eV and stemming from direct transitions along Γ -*M* and Γ -*X*, is significantly higher than the until now reported optical absorption onset of about 6.5 eV. We suggested this can be explained by a combination of finite temperature renormalization effects on the gap due to electron-phonon coupling and strong excitonic effects in this ionic material. A fuller investigation of these effects will require additional work in the future. For future use, we have provided details of the band structure near the band edges, including the effective masses. We have also briefly discussed the possibility of silicon as a donor for γ -LiAlO₂, which indicates that *n*-type doping should be possible although efficient doping will be challenging due to the relatively high donor binding energy.

ACKNOWLEDGMENTS

This work made use of the High Performance Computing Resource in the Core Facility for Advanced Research Computing at Case Western Reserve University. This work was supported by the U.S. Department of Energy, Basic Energy Sciences, under Grant No. DE-SC0008933 and a student travel grant from CWRU SOURCE.

- [1] S.-G. Ma, T. Gao, S.-C. Li, X.-J. Ma, Y.-H. Shen, and T.-C. Lu, Theoretical investigations on the α -LiAlO₂ properties via first-principles calculation, *Fusion Eng. Des.* **113**, 324 (2016).
- [2] R. R. Vanfleet, J. A. Simmons, D. W. Hill, M. M. C. Chou, and B. H. Chai, Antiphase ordering and surface phases in lithium aluminate, *J. Appl. Phys.* **104**, 093530 (2008).
- [3] M. Marezio, The crystal structure and anomalous dispersion of γ -LiAlO₂, *Acta Crystallogr.* **19**, 396 (1965).

- [4] X. Li, T. Kobayashi, F. Zhang, and K. Kimoto, A new high-pressure phase of LiAlO₂, *J. Solid State Chem.* **177**, 1939 (2004).
- [5] L. Lei, D. He, Y. Zou, W. Zhang, Z. Wang, M. Jiang, and M. Du, Phase transitions of LiAlO₂ at high pressure and high temperature, *J. Solid State Chem.* **181**, 1810 (2008).
- [6] <http://www.materialsproject.org/>.

- [7] J. Charpin, F. Botter, M. Bricc, B. Rasneur, E. Roth, N. Roux, and J. Sannier, Investigation of γ lithium aluminate as tritium breeding material for a fusion reactor blanket, *Fusion Eng. Des.* **8**, 407 (1989).
- [8] R. B. Khomane, A. Agrawal, and B. D. Kulkarni, Synthesis and characterization of lithium aluminate nanoparticles, *Mater. Lett.* **61**, 4540 (2007).
- [9] V. Batra, S. Maudgal, S. Bali, and P. Tewari, Development of alpha lithium aluminate matrix for molten carbonate fuel cell, *J. Power Sources* **112**, 322 (2002).
- [10] X. Ke, X. Jun, D. Peizhen, Z. Yongzong, Z. Guoqing, Q. Rongsheng, and F. Zujie, γ -LiAlO₂ single crystal: A novel substrate for GaN epitaxy, *J. Cryst. Growth* **193**, 127 (1998).
- [11] A. Boonchun and W. R. L. Lambrecht, Electronic structure, doping, and lattice dynamics of LiGaO₂, in *Oxide-Based Materials and Devices II*, edited by F. H. Teherani, D. C. Look, and D. J. Rogers (SPIE, Bellingham, WA, 2011), Vol. 7940, pp. 129–134.
- [12] A. Boonchun, K. Dabsamut, and W. R. L. Lambrecht, First-principles study of point defects in LiGaO₂, *J. Appl. Phys.* **126**, 155703 (2019).
- [13] C. A. Lenyk, M. S. Holston, B. E. Kananen, L. E. Halliburton, and N. C. Giles, Lithium and gallium vacancies in LiGaO₂ crystals, *J. Appl. Phys.* **124**, 135702 (2018).
- [14] D. Skachkov, W. R. L. Lambrecht, K. Dabsamut, and A. Boonchun, Computational study of electron paramagnetic resonance spectra for Li and Ga vacancies in LiGaO₂, *J. Phys. D* **53**, 17LT01 (2020).
- [15] K. Dabsamut, A. Boonchun, and W. R. L. Lambrecht, First-principles study of *n*- and *p*-type doping opportunities in LiGaO₂, *J. Phys. D* **53**, 274002 (2020).
- [16] I. Ohkubo, C. Hirose, K. Tamura, J. Nishii, H. Saito, H. Koinuma, P. Ahemt, T. Chikyow, T. Ishii, S. Miyazawa, Y. Segawa, T. Fukumura, and M. Kawasaki, Heteroepitaxial growth of β -LiGaO₂ thin films on ZnO, *J. Appl. Phys.* **92**, 5587 (2002).
- [17] J. T. Wolan and G. B. Hoflund, Chemical alteration of the native oxide layer on LiGaO₂(001) by exposure to hyperthermal atomic hydrogen, *J. Vacuum Sci. Technol. A* **16**, 3414 (1998).
- [18] C. Chen, C.-A. Li, S.-H. Yu, and M. M. Chou, Growth and characterization of β -LiGaO₂ single crystal, *J. Cryst. Growth* **402**, 325 (2014).
- [19] N. W. Johnson, J. A. McLeod, and A. Moewes, The electronic structure of lithium metagallate, *J. Phys.: Condens. Matter* **23**, 445501 (2011).
- [20] M. van Schilfhaarde, T. Kotani, and S. Faleev, Quasiparticle Self-Consistent GW Theory, *Phys. Rev. Lett.* **96**, 226402 (2006).
- [21] S. K. Radha, A. Ratnaparkhe, and W. R. L. Lambrecht, Quasiparticle self-consistent GW band structures and high-pressure phase transitions of LiGaO₂ and NaGaO₂, *Phys. Rev. B* **103**, 045201 (2021).
- [22] H. Cao, B. Xia, Y. Zhang, and N. Xu, LiAlO₂-coated LiCoO₂ as cathode material for lithium ion batteries, *Solid State Ionics* **176**, 911 (2005).
- [23] D. Wiedemann, S. Nakhil, J. Rahn, E. Witt, M. M. Islam, S. Zander, P. Heitjans, H. Schmidt, T. Bredow, M. Wilkening, and M. Lerch, Unravelling ultraslow lithium-ion diffusion in γ -LiAlO₂: Experiments with tracers, neutrons, and charge carriers, *Chem. Mater.* **28**, 915 (2016).
- [24] D. Wiedemann, S. Indris, M. Meven, B. Pedersen, H. Boysen, R. Uecker, P. Heitjans, and M. Lerch, Single-crystal neutron diffraction on γ -LiAlO₂: Structure determination and estimation of lithium diffusion pathway, *Z. Kristallogr. Crystalline Mater.* **231**, 189 (2016).
- [25] G. Ceder, Y.-M. Chiang, D. R. Sadoway, M. K. Aydinol, Y.-I. Jang, and B. Huang, Identification of cathode materials for lithium batteries guided by first-principles calculations, *Nature (London)* **392**, 694 (1998).
- [26] M. A. K. Lakshman Dissanayake, Nano-composite solid polymer electrolytes for solid state ionic devices, *Ionics* **10**, 221 (2004).
- [27] B. Singh, M. K. Gupta, R. Mittal, and S. L. Chaplot, Phonons, phase transitions and thermal expansion in LiAlO₂: An ab initio density functional study, *Phys. Chem. Chem. Phys.* **20**, 12248 (2018).
- [28] W. Sailuam, K. Sarasamak, and S. Limpijumngong, High pressure phase of LiAlO₂: A first principles study, *Integr. Ferroelectr.* **156**, 15 (2014).
- [29] T. Huang, S. Zhou, H. Teng, H. Lin, J. Zou, J. Zhou, and J. Wang, Growth and characterization of high-quality LiAlO₂ single crystal, *J. Mater. Sci. Technol.* **24**, 145 (2008).
- [30] J. Zou, S. Zhou, J. Xu, L. Zhang, Z. Xie, P. Han, and R. Zhang, Influence of vapor transport equilibration on the crystal quality and thermal-expansion coefficients of γ -LiAlO₂, *J. Appl. Phys.* **98**, 084909 (2005).
- [31] M. Holston, J. McClory, N. Giles, and L. Halliburton, Radiation-induced defects in LiAlO₂ crystals: Holes trapped by lithium vacancies and their role in thermoluminescence, *J. Lumin.* **160**, 43 (2015).
- [32] M. Holston, I. Ferguson, N. Giles, J. McClory, and L. Halliburton, Identification of defects responsible for optically stimulated luminescence (OSL) from copper-diffused LiAlO₂ crystals, *J. Lumin.* **164**, 105 (2015).
- [33] J. Jimenez-Becerril and I. García-Sosa, Synthesis of lithium aluminate by thermal decomposition of a lithium dawsonite-type precursor, *J. Ceram. Process. Res.* **12**, 52 (2011).
- [34] <https://jp-minerals.org/vesta/en/>.
- [35] <https://www.questaal.org/docs/>.
- [36] P. Giannozzi, S. Baroni, N. Bonini, M. Calandra, R. Car, C. Cavazzoni, D. Ceresoli, G. L. Chiarotti, M. Cococcioni, I. Dabo, A. D. Corso, S. de Gironcoli, S. Fabris, G. Fratesi, R. Gebauer, U. Gerstmann, C. Gougoussis, A. Kokalj, M. Lazzeri, L. Martin-Samos *et al.*, QUANTUMESPRESSO: A modular and open-source software project for quantum simulations of materials, *J. Phys.: Condens. Matter* **21**, 395502 (2009).
- [37] P. E. Blöchl, Projector augmented-wave method, *Phys. Rev. B* **50**, 17953 (1994).
- [38] J. P. Perdew, K. Burke, and M. Ernzerhof, Generalized Gradient Approximation Made Simple, *Phys. Rev. Lett.* **77**, 3865 (1996).
- [39] F. Birch, Finite elastic strain of cubic crystals, *Phys. Rev.* **71**, 809 (1947).
- [40] D. Pashov, S. Acharya, W. R. Lambrecht, J. Jackson, K. D. Belashchenko, A. Chantis, F. Jamet, and M. van Schilfhaarde, QUESTAAL: A package of electronic structure methods based on the linear muffin-tin orbital technique, *Comput. Phys. Commun.* **249**, 107065 (2020).

- [41] L. Hedin, New method for calculating the one-particle Green's function with application to the electron-gas problem, *Phys. Rev.* **139**, A796 (1965).
- [42] B. Cunningham, M. Grüning, P. Azarhoosh, D. Pashov, and M. van Schilfgaarde, Effect of ladder diagrams on optical absorption spectra in a quasiparticle self-consistent GW framework, *Phys. Rev. Mater.* **2**, 034603 (2018).
- [43] B. Cunningham, M. Gruening, D. Pashov, and M. van Schilfgaarde, QSGW: Quasiparticle self consistent GW with ladder diagrams in W, [arXiv:2106.05759](https://arxiv.org/abs/2106.05759).
- [44] D. Deguchi, K. Sato, H. Kino, and T. Kotani, Accurate energy bands calculated by the hybrid quasiparticle self-consistent GW method implemented in the ECALJ package, *Jpn. J. Appl. Phys.* **55**, 051201 (2016).
- [45] C. Bhandari, M. van Schilfgaarde, T. Kotani, and W. R. L. Lambrecht, All-electron quasiparticle self-consistent GW band structures for SrTiO₃ including lattice polarization corrections in different phases, *Phys. Rev. Mater.* **2**, 013807 (2018).
- [46] S. Limpijumnong and W. R. L. Lambrecht, Homogeneous Strain Deformation Path for the Wurtzite to Rocksalt High-Pressure Phase Transition in GaN, *Phys. Rev. Lett.* **86**, 91 (2001).
- [47] <https://www.cryst.ehu.es/>.
- [48] F. Mehnke, T. Wernicke, H. Pingel, C. Kuhn, C. Reich, V. Kueller, A. Knauer, M. Lapeyrade, M. Weyers, and M. Kneissl, Highly conductive n-Al_xGa_{1-x}N layers with aluminum mole fractions above 80%, *Appl. Phys. Lett.* **103**, 212109 (2013).
- [49] O. Dernek, D. Skachkov, W. R. L. Lambrecht, and M. van Schilfgaarde, Real space representation of the quasiparticle self-consistent GW self-energy and its application to defect calculations, *Phys. Rev. B* **105**, 205136 (2022).